ARTICLE

Boosting Bisphenol A Degradation through Activation of Persulfate by Iron-doped γ-MnO_2

Yucheng Shao, Yuyang Gan, Jinze Xu, Xiyang Zheng, Xiao Ge*

College of Environmental Science and Engineering, Yangzhou University, Yangzhou 225000, China

(Dated: Received on December 18, 2024; Accepted on April 14, 2025)

The iron-doped γ-MnO_2 catalyst (Fe-MnO_2) was successfully prepared using a one-pot co-precipitation method. Morphological and structural characterization, indicated that iron elements were uniformly incorporated into the γ-MnO_2 lattice without the emergence of iron oxide peaks.

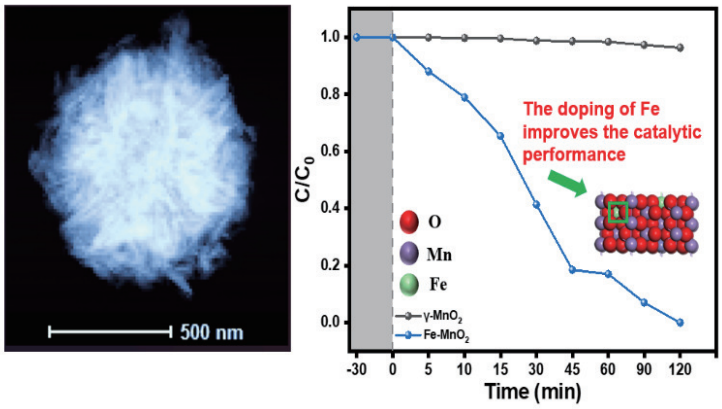

The prepared Fe-MnO_2 exhibited superior performance in activating peroxydisulfate(PDS) for the degradation of bisphenol A (BPA) compared to pure γ-MnO_2. The process can efficiently remove 10 ppm of BPA within 120 min, achieving a pseudo-first-order kinetic constant (k) of 0.0301 min^{-1}, which was approximately 100 times higher than that of pure γ-MnO_2. The Fe-MnO_2 catalyst demonstrated excellent PDS activation capabilities, providing a significant amount of non-radical $^1O_2$ for the advanced oxidation reaction system. The high concentration of non-radical $^1O_2$ reacted with BPA, leading to its degradation. Additionally, the Fe-MnO_2 catalyst displayed good stability, maintaining its activity and achieving complete degradation of 10 ppm of BPA even after five cycles of experiments. Its effectiveness in removing pollutants remained unaffected under neutral and acidic pH conditions, making it a viable option for BPA degradation.

Key words: Endocrine disrupting chemicals, Bisphenol A degradation, Persulfates, Advanced oxidation processes, Reactive oxidant species

I. INTRODUCTION

Endocrine disrupting chemicals (EDCs) which are harmful substances, can disrupt the endocrine system of animals and impact their reproductive development. These chemicals have been frequently detected in surface water and soil in recent years. Studies indicate that EDCs not only exhibit high toxicity to aquatic organisms but also pose threats to human health [1]. Their adverse effects are primarily observed in the reproductive and nervous systems [2], leading to conditions such as obesity [3], diabetes [4], infertility, and even severe diseases like breast cancer and testicular cancer [5]. Among these EDCs, bisphenol A (BPA) stands out as a typical example, widely used in the production of polycarbonate plastics and epoxy resins [6]. However, it is challenging to remove it using conventional pollution treatment techniques due to its low vapor pressure, low water solubility, and low volatility [7].

* Author to whom correspondence should be addressed.
E-mail: gexiao@ustc.edu.cn

 © 2025 Chinese Physical Society

Current treatment methods for BPA include physical adsorption, chemical oxidation, and biodegradation. Among these, chemical oxidation methods encompass various techniques, including advanced oxidation processes (AOPs) [8]. AOPs, in particular, have gained popularity for BPA degradation due to their simplicity, absence of secondary pollution, and cost-effectiveness. These processes involve techniques like ozonation, Fenton-like reactions, photocatalytic degradation, and persulfate activation [9]. Their effectiveness lies in the generation of reactive oxidant species (ROS), which can rapidly and efficiently degrade organic pollutants. ROS are primarily produced through oxidants such as peroxydisulfate (PDS), peroxymonosulfate (PMS), and hydrogen peroxide [10, 11], relying on energy transfer and electrons [12] provided by catalysts [13, 14].

PDS, a commonly used reagent for the degradation of pollutants, can be activated through various methods such as heating, ultrasonication, illumination, and transition metals, generating a range of radicals and non-radicals. The choice of PDS in this study was based on its higher reactivity and efficiency in generating sulfate radicals under our specific experimental conditions. Moreover, PDS has shown a broader pH range of effectiveness and better stability compared to PMS. Despite these advantages, the need for efficient, economical, and environmentally friendly PDS activation methods remains crucial, as the redox potentials of these radicals and non-radicals exceed that of PDS itself [15]. Typically, PDS is activated by Fe^{2+}, heat, or ultraviolet light, which requires a higher activation energy. However, when combined with iron-containing catalysts, the process becomes more economical and environmentally friendly [16–19].

In recent years, manganese oxides and their composites have emerged as effective adsorbents and catalysts for removing organic pollutants from wastewater [20–25]. These materials offer advantages such as a large specific surface area, a porous structure, numerous active sites, good thermal stability, easy recyclability, high environmental compatibility, and low toxicity [26–29]. However, for certain hard-to-degrade substances, manganese dioxide may not perform optimally in terms of its specific surface area, crystal structure, and oxygen-manganese binding strength. To overcome these limitations, researchers have made improvements to manganese dioxide, exploring its combinations with other materials [30–33].

Based on these advancements, we propose the synthesis of a functional material combining Fe and Mn oxides. This material aims to harness the strengths of both metal elements, exhibiting significant potential for degrading challenging organic pollutants [34, 35]. To achieve this, we developed a simple and efficient synthesis method that does not rely on sacrificial templates. Through a one-step redox reaction between Mn(II)/Fe(II) precursors and ammonium persulfate, we successfully prepared an iron-doped manganese dioxide catalyst. This catalyst features more active sites on its surface and stronger oxidizing ability compared to pure γ-MnO_2. It effectively adsorbs PDS molecules, enabling reactions on its surface to generate abundant radicals and non-radicals. These reactive species interact with BPA, leading to its degradation and ultimate conversion into water and carbon dioxide. Our study not only investigated the morphological and structural characteristics of these microspheres but also tested their efficacy in removing BPA from contaminated water bodies, highlighting their significant potential in catalytic degradation of BPA in polluted water.

II. EXPERIMENTS

A. Reagents

Ferrous sulfate heptahydrate ($FeSO_4 \cdot 7H_2O$), manganese chloride tetrahydrate ($MnCl_2 \cdot 4H_2O$), ammonium persulfate ($(NH_4)_2S_2O_8$), sodium persulfate ($Na_2S_2O_8$), L-histidine, tert-butanol, methanol (MeOH), sodium hydroxide (NaOH), hydrochloric acid (HCl), sodium chloride (NaCl), magnesium chloride ($MgCl_2$), potassium chloride (KCl), sodium sulfate (Na_2SO_4), sodium carbonate (Na_2CO_3), sodium bicarbonate ($NaHCO_3$), and sodium dihydrogen phosphate (NaH_2PO_4) were provided by Sinopharm Chemical Reagent Co., Ltd. (Shanghai, China). Bisphenol A (BPA) and 1,4-benzoquinone were supplied by Aladdin Chemistry Co., Ltd. (Shanghai, China). All the chemical reagents were of analytical grade and used without further purification in the experiments, and the chemical solutions were prepared using deionized water.

B. Preparation of Fe-MnO_2 catalyst

The Fe-MnO_2 catalysts with varying iron contents were synthesized using a one-pot co-precipitation method. Initially, 4.5 mmol of $MnCl_2$ and 5 mmol of $(NH_4)_2S_2O_8$ were dissolved in 40 mL of deionized water.

DOI: 10.1063/1674-0068/cjcp2412159 © 2025 Chinese Physical Society

This mixture underwent a brief ultrasonic treatment to guarantee homogeneity. The prepared solution was then transferred to a round-bottom flask, where it was magnetically stirred and steadily heated to 80 °C in a water bath. Once a significant amount of black precipitate formed, 10 mL of 200 mmol/L $FeSO_4$ solution was introduced. Following a six-hour reaction period, the precipitate was separated via centrifugation and thoroughly washed with deionized water and ethanol. The final product was dried in a vacuum oven at 60 °C for subsequent applications.

For comparative purposes, pure γ-MnO_2 was produced using the same procedure, omitting the addition of $FeSO_4$. Catalysts with iron contents of 5%, 15%, and 30% were also synthesized by adjusting the concentration of the $FeSO_4$ solution accordingly. In this study, Fe-MnO_2 specifically denotes the catalyst with a 10% iron content, while the catalysts with 5%, 15%, and 30% iron contents are designated as Fe-MnO_2-5, Fe-MnO_2-15, and Fe-MnO_2-30, respectively.

C. Degradation experiment of BPA

The removal efficiency of bisphenol A (BPA) by the Fe-MnO_2/PDS system was evaluated through degradation experiments. Both the BPA solution and the PDS solution were prepared freshly for each experiment. Specifically, 50 mL of a prepared 10 ppm BPA solution was poured into a beaker, and then 10 mg of the previously synthesized catalyst sample was accurately weighed and added to the BPA solution. Ultrasonic vibration was applied to ensure the uniform dispersion of the catalyst within the solution. The beaker was then placed on a centrifugal stirrer and stirred at a speed of 200 r/min. After 30 min stirring, the first sample was taken to assess adsorption. Following this, 1 mL of a 0.2 g/L PDS solution was added, and samples were collected at specific time intervals. For each sample, 0.5 mL was precisely withdrawn using a pipette and filtered through a 0.45-μm filter to remove the catalyst. The filtered sample was then mixed with 0.5 mL of methanol (CH_3OH) to halt further degradation. Finally, the samples were transferred to brown vials for high-performance liquid chromatography (HPLC) analysis.

In experiments involving variations in pH, the pH of the BPA solution was adjusted using HCl or NaOH solutions. For quenching experiments, the quenching agents were added to the BPA solution prior to the addition of PDS. The concentrations of methanol and tert-butanol as quenching agents were 200 mmol/L, while L-histidine and 1,4-benzoquinone were used at 20 mmol/L. In ion influence experiments, the concentration of the ions in the contaminant solution was maintained at 10 mmol/L. All the final samples were analyzed using HPLC.

D. Analytical methods

BPA was determined using HPLC with a C18 column (1.7 μm, 2.1 × 100 mm) and a UV detector set at 280 nm. The mobile phase consisted of 70% methanol (labeled as A) and 30% water (labeled as B), with a flow rate of 0.2 mL/min and a column temperature of 30 °C for the separation and analysis of analytes.

III. RESULTS AND DISCUSSION

A. Microstructural analysis

The morphological and structural characteristics of the Fe-MnO_2 samples were comprehensively investigated. FIG. 1(a) illustrates the step-by-step synthesis of Fe-MnO_2 microspheres. In the process of synthesizing γ-MnO_2 via water bath heating, iron from $FeSO_4$ was seamlessly integrated into the γ-MnO_2 crystal lattice, maintaining the integrity of the original crystal structure [36]. As shown in FIG. 1(b), the resulting samples exhibit a spherical morphology with diameters varying within the range of hundreds of nanometers. High-resolution transmission electron microscopy (HRTEM) images, particularly FIG. 1(c) and FIG. 1(e), reveal two different lattice spacing patterns on the surface of the material. Enlarge these two figures further to get FIG. 1(d) and FIG. 1(f). Upon closer examination in FIG. 1(d) and FIG. 1(f), distinct lattice spacings of 0.164 nm, 0.142 nm, and 0.242 nm are identified, corresponding to the (160), (421), and (131) planes of γ-MnO_2, respectively. Furthermore, the incorporation of iron elements is evident through the presence of regions with different color on the γ-MnO_2 surface. Additionally, high-angle annular dark-field scanning transmission electron microscopy (HAADF-STEM) images, combined with energy-dispersive X-ray spectroscopy (EDS) mappings, demonstrate the uniform distribution of Mn, O, and Fe elements within the microspheres.

Specifically, Mn (represented by yellow regions), O (indicated by red areas), and Fe (highlighted in green zones) are evenly dispersed throughout the entire spherical structure, as seen in FIG. 1(g). This observation

DOI: 10.1063/1674-0068/cjcp2412159 © 2025 Chinese Physical Society

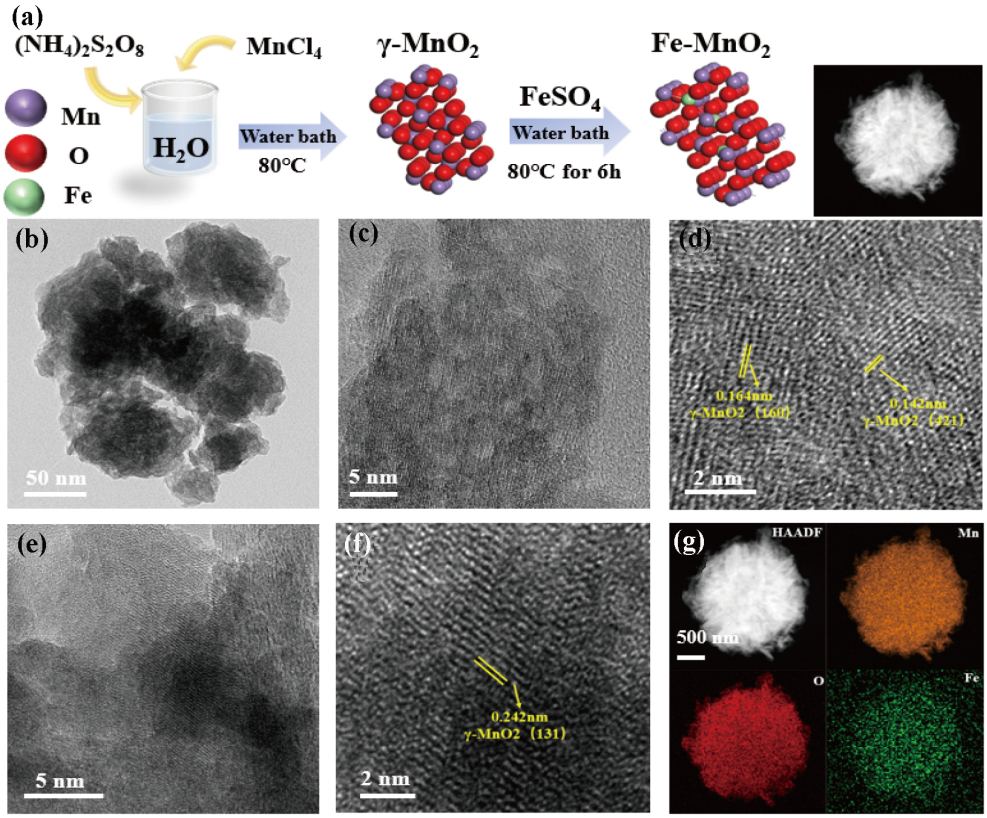

FIG. 1 (a) Schematic diagram of the synthesis of Fe-MnO_2 microspheres. (b) TEM image of Fe-MnO_2. (c–f) HRTEM images of Fe-MnO_2; (c) and (e) are two different sections; (d) and (f) are magnification of (c) and (e) respectively. (g) EDS and mapping images of Fe-MnO_2.

strongly supports the homogeneous doping of Fe within the γ-MnO_2 matrix. The prepared samples, distinguished by their spherical micro/nanostructures and abundant active sites, are expected to enhance the activation of PDS, ultimately promoting the efficient degradation of bisphenol A.

The purity and crystalline structure of the synthesized products were analyzed through X-ray diffraction (XRD). Referring to FIG. 2(a), the Fe-MnO_2 sample exhibited peaks that correspond precisely to those observed in pure γ-MnO_2. These peaks, detected at 22.43°, 37.12°, 42.61°, 56.41°, and 65.6°, are attributed to the (120), (131), (300), (160), and (421) planes of γ-MnO_2, respectively, aligning with the standard card 14#-0644 [37, 38]. Notably, despite the introduction of Fe, no additional peaks indicating iron oxide were present in the XRD pattern, suggesting that γ-MnO_2 maintained the overall crystal structure. However, a slight shift towards smaller angles in the XRD diffraction peaks indicates successful Fe doping within the γ-MnO_2 crystal structure.

To further validate the integration of Fe into the γ-MnO_2 framework, Raman spectroscopy was employed to investigate lattice vibration behaviors. As evident from FIG. 2(b), pure γ-MnO_2 displays a prominent peak at approximately 650 cm^{-1}, corresponding to the lattice vibration of O-Mn-O. Upon Fe doping, this peak becomes broader and less distinct, indicating a reduction in both sample size and crystallinity. Importantly, no Fe–O bond peaks were detected in the spectrum, further supporting the successful doping of Fe into γ-MnO_2 without altering its fundamental structure.

Additionally, Fourier transform infrared spectroscopy (FT-IR) was utilized to assess the impact of Fe doping on the functional groups of γ-MnO_2. As shown in FIG. 2(c), γ-MnO_2 exhibits peaks at 443.5 and 694.2 cm^{-1}, representing the stretching vibration mode of Mn-O-Mn [39, 40]. These peaks persist, with slight increases in intensity upon Fe doping, suggesting an effect on the Mn-O-Mn stretching vibration. Moreover, peaks near 1106.7 and 1427.1 cm^{-1} correspond to surface -OH groups of Mn-OH, while the peak at 1635.3 cm^{-1} indicates adsorbed water bending [41–43]. These peaks undergo minor changes but remain present with Fe doping. Notably, a prominent peak emerges in the range of 3000–3500 cm^{-1}, likely representing ad-

DOI: 10.1063/1674-0068/cjcp2412159 © 2025 Chinese Physical Society

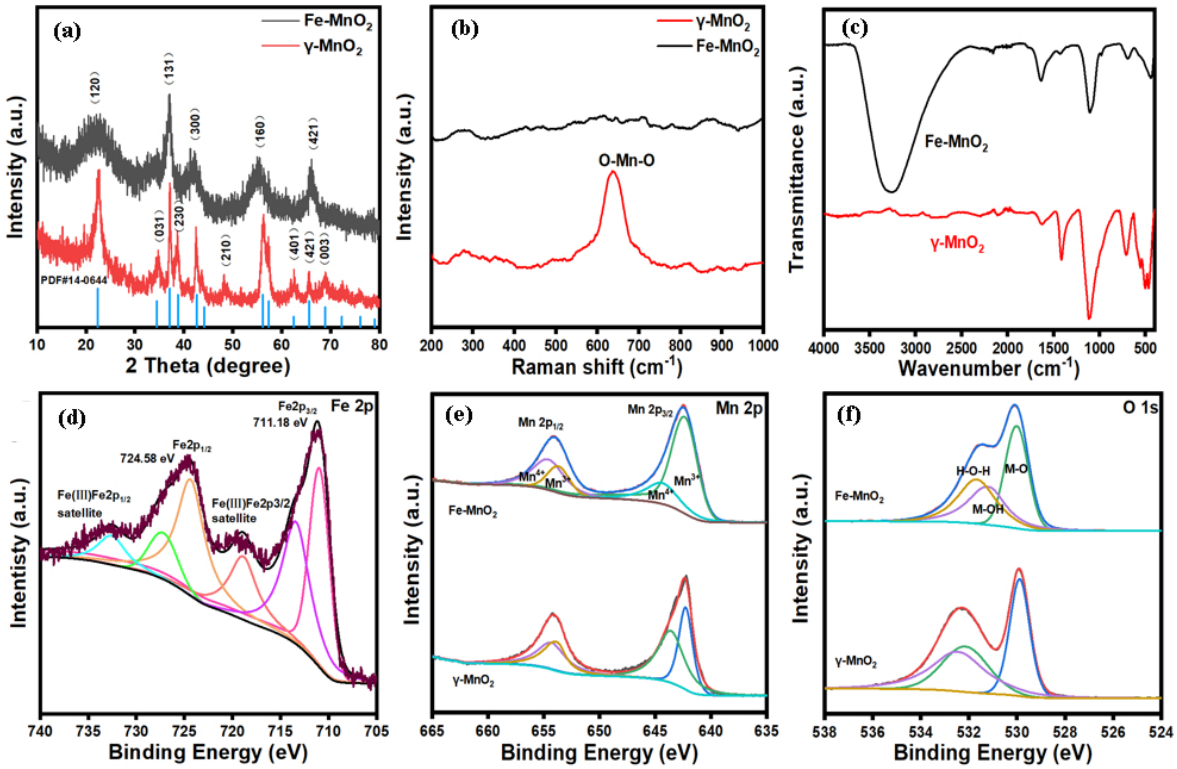

FIG. 2 (a) XRD images of the prepared samples. (b) Raman spectra of the prepared samples. (c) Fourier transform infrared spectroscopy (FT-IR) of the prepared samples. (d–f) XPS images of the prepared samples, showing Fe 2p, Mn 2p, and O 1s.

sorbed water and hydroxyl absorption, which may contribute to the enhanced PDS activation capability of the doped sample.

Finally, X-ray photoelectron spectroscopy (XPS) was conducted to elucidate the influence of Fe doping on the electronic and chemical states of γ-MnO_2. An analysis of the Fe 2p XPS spectrum (FIG. 2(d)) revealed characteristic peaks at 711.1 eV and 724.7 eV, corresponding to Fe $2p_{3/2}$ and Fe $2p_{1/2}$, respectively, along with satellite peaks at 719.5 eV and 732.4 eV. This suggests that Fe primarily exists in the sample as Fe(III) and Fe(II). Examination of the Mn 2p XPS spectrum (FIG. 2(e)) indicated that Fe doping may have altered the chemical state of Mn, as evidenced by shifts in the binding energies of Mn $2p_{3/2}$ peaks [44]. In FIG. S1 (Supplementary materials, SM), comparative analysis of the Mn 2p XPS spectra before and after degradation reveals a discernible decrease in the proportion of Mn (IV) post-reaction. This observation demonstrates that Mn (IV) species function as potent oxidants, facilitating electron transfer through valence state transitions during the catalytic process. The diminished Mn (IV) concentration after the reaction completion underscores its active participation in redox reactions, where it undergoes reduction while promoting substrate oxidation. Furthermore, an analysis of the O 1s XPS spectrum (FIG. 2(f)) showed a significant decrease in the intensity of the higher binding energy peak in γ-MnO_2 upon Fe doping, potentially due to a reduction in Mn-OH.

B. Degradation of BPA in the Fe-MnO_2/PDS system

We investigated the degradation efficiency of BPA pollutants using Fe-MnO_2 samples activated with PDS, targeting BPA at a concentration of 10 ppm. FIG. 3(a) reveals that Fe-doped Fe-MnO_2 exhibits remarkable PDS activation capability, significantly enhancing the degradation efficiency of BPA compared to γ-MnO_2. Among various Fe content samples, Fe-MnO_2 demonstrated the most outstanding BPA degradation performance, achieving a 100% degradation rate within 120 min. However, deviations from this optimal Fe content led to relatively lower degradation efficiencies. Specifically, Fe-MnO_2-5 resulted in a 57.5% degradation rate, while Fe-MnO_2-15 achieved an 89.1% rate within the same timeframe. Although the latter is better than γ-MnO_2 without Fe doping, it still doesn't match the op-

DOI: 10.1063/1674-0068/cjcp2412159 © 2025 Chinese Physical Society

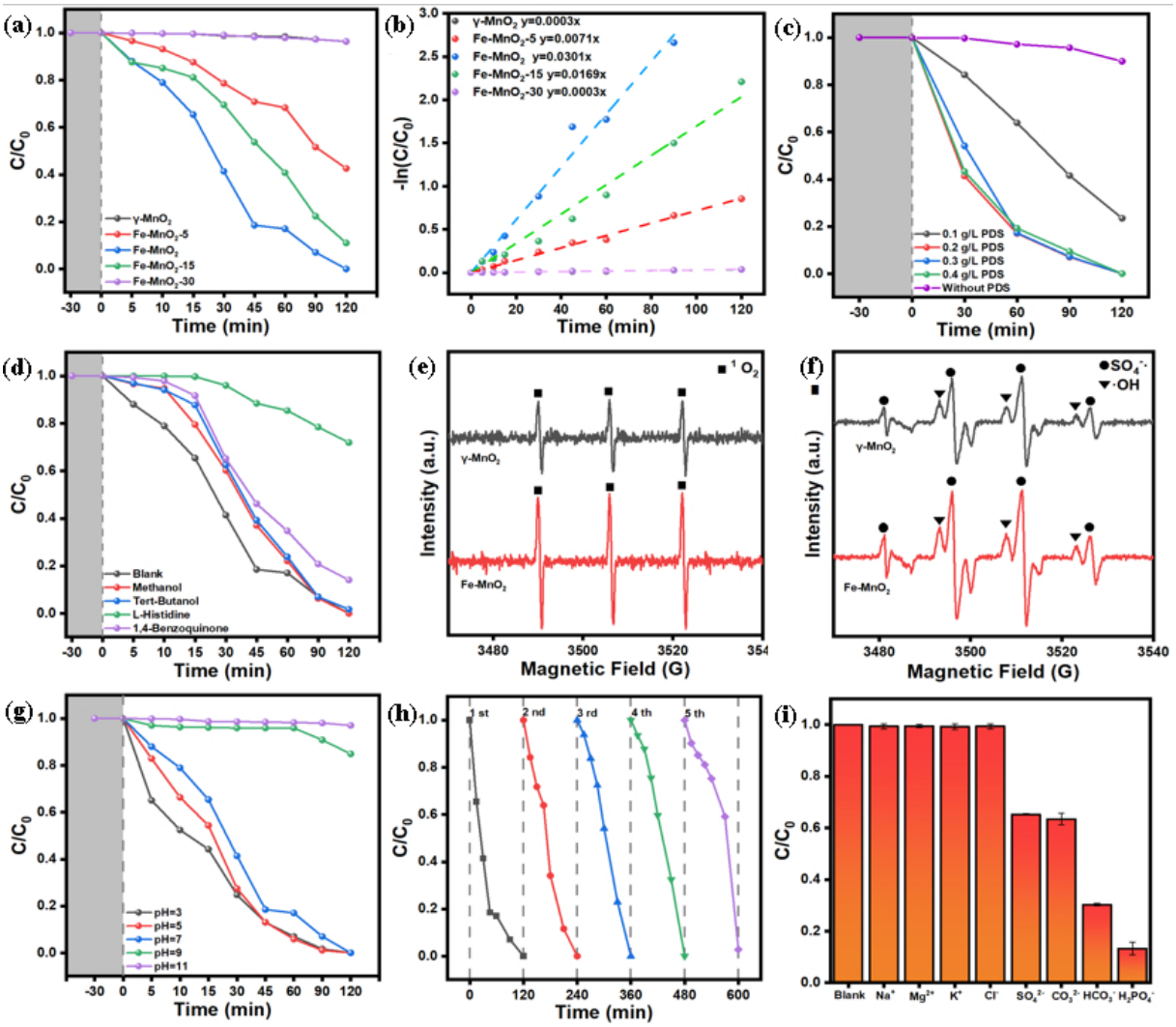

FIG. 3 (a) The degradation efficiency of Fe-MnO_2 activated PDS at 10 ppm of BPA. (b) The first-order kinetic curve of Fe-MnO_2 activated PDS degradation efficiency for BPA. (c) The curve of BPA degradation efficiency with different concentrations of PDS. (d) The degradation efficiency curve with the addition of different quenching reagents. (e, f) The EPR spectra of DMPO-SO_4^{-}·, ·OH, and TEMP-$^1O_2$. (g) The BPA degradation efficiency curve under different pH environments. (h) The cycling experiment. (i) The degradation efficiency with the addition of different influencing ions through a bar chart. Conditions: [BPA]=10 ppm, [PDS]= 200 ppm except (c), pH=7 except (g), [methanol]=200 mmol/L, [tert-butanol]= 200 mmol/L, [L-histidine]=20 mmol/L, [1,4-benzoquinone]=20 mmol/L, and the ion concentrations in (i) are all 10 mmol/L.

timal performance. Furthermore, increasing the Fe content to 30% led to a decline in degradation performance, similar to that of γ-MnO_2 without Fe doping. This phenomenon may be primarily attributed to two factors. First, excess Fe tends to form agglomerations during the reaction, preventing its complete incorporation into the MnO_2 crystal lattice. Second, surplus Fe may promote the formation of iron oxide, which exhibits significantly lower catalytic activity compared to MnO_2. These factors collectively contribute to a reduction in the overall catalytic performance of the system.

Comparative analysis of total organic carbon (TOC) removal efficiencies was performed for Fe-MnO_2 and pure γ-MnO_2 catalysts. The data demonstrate a substantial enhancement in catalytic performance following iron incorporation, with TOC removal rates increasing from 15.67% to 66.73%. This marked improvement underscores the beneficial effect of Fe doping on the catalyst's oxidative capacity and overall reaction efficiency (Table S1 in SM).

Calculation of the pseudo-first-order kinetic constant (k) from FIG. 3(b) shows that the k value of Fe-MnO_2 is approximately 100 times higher than that of pure γ-MnO_2, reaching 0.0301 min^{-1}. The k values for

DOI: 10.1063/1674-0068/cjcp2412159 © 2025 Chinese Physical Society

Fe-MnO_2-5 and Fe-MnO_2-15 are 0.0071 min^{-1} and 0.0169 min^{-1}, respectively. Although these values are lower than that of Fe-MnO_2, they are still significantly higher than that of pure γ-MnO_2. The k value for Fe-MnO_2-30 is nearly indistinguishable from that of pure γ-MnO_2.

We also examined the optimal PDS concentration for the catalytic system (FIG. 3(c)). A PDS concentration of 0.2 g/L was found to be sufficient for complete BPA degradation within 120 min. Reducing the PDS concentration to 0.1 g/L resulted in a significant decrease in efficiency, with approximately 23.4% of the BPA remaining after 120 min. Increasing the PDS concentration beyond 0.2 g/L did not further improve degradation efficiency.

FIG. S2 in SM presents the investigation into optimal catalyst loading, where the findings indicate that 0.2 g/L represents the most effective concentration. Notably, exceeding this loading threshold yields no substantial improvement in overall degradation efficiency.

Furthermore, Table S2 in SM provides a comparative analysis of Fe-MnO_2 performance with that of recently reported catalytic systems. The data demonstrate that Fe-MnO_2 exhibits notably superior bisphenol A (BPA) degradation capabilities, surpassing contemporary benchmark catalysts in oxidative efficiency. This comparative assessment underscores the advanced catalytic activity of the iron-doped manganese dioxide formulation.

To elucidate the mechanism of pollutant degradation, we introduced various quenchers into the reaction system to identify the reactive species involved [45]. As illustrated in FIG. 3(d), the addition of L-histidine significantly inhibited BPA degradation, reducing the degradation efficiency from 100% to 28% after 120 min. This finding indicates that singlet oxygen ($^1O_2$) plays a pivotal role in the degradation process. Electron paramagnetic resonance (EPR) testing confirmed the generation of singlet oxygen by both γ-MnO_2 and Fe-MnO_2 upon PDS activation. The $^1O_2$ was detected using 2,2,6,6-tetramethylpiperidine (TEMP) as the capture agent. The $SO_4^{-}\cdot$ and $\cdot OH$ were detected using 5,5-dimethyl-1-pyrroline N-oxide (DMPO) as the capture agent. In a separate experiment, we detected $^1O_2$ signals in both γ-MnO_2 and Fe-MnO_2 reaction systems, with Fe-MnO_2 producing a stronger signal (FIG. 3(e)). This suggests that Fe-MnO_2 generates a higher amount of $^1O_2$ compared to γ-MnO_2 [46–48]. Although both systems also showed signals of sulfate radicals (FIG. 3(f)), their role appeared less significant as the addition of methanol to quench these radicals did not inhibit BPA degradation [49].

We further investigated the performance of the Fe-MnO_2 reaction system under different pH conditions (FIG. 3(g)). The system performed optimally under neutral and acidic conditions (pH 3–7), completely degrading BPA within 120 min. However, alkaline conditions hindered the reaction progress. Additionally, Fe-MnO_2 demonstrated excellent stability and reusability, maintaining its degradation efficiency even after five consecutive cycles (FIG. 3(h)).

Finally, we explored the influence of common ions on the degradation process (FIG. 3(i)). While Na^+, Mg^{2+}, K^+, and Cl^- ions had no significant effect, SO_4^{2-}, CO_3^{2-}, HCO_3^-, and $H_2PO_4^-$ ions affected the reaction to varying degrees. These anions are likely to react with free radicals, generating less active species and thus reducing degradation efficiency [50]. Among them, SO_4^{2-} is a product of persulfate decomposition. However, when the concentration of SO_4^{2-} is too high, it may affect the reaction progress. For instance, it can inhibit the decomposition of persulfate through the common ion effect or form complexes with metal ions during metal activation, thereby changing the activity of the catalyst. Despite this, SO_4^{2-} as a background electrolyte still has a relatively small effect on the reaction unless its concentration is very high. In addition, $H_2PO_4^-$ may form precipitates or complexes with Fe^{2+} or Fe^{3+} in the catalyst, thereby reducing catalyst activity. CO_3^{2-} and HCO_3^- are buffering agents in water, but they can also act as scavengers for free radicals. They react with $SO_4^{-}\cdot$ to generate $CO_3^{-}\cdot$, which reduces the oxidation capacity and thus decreases the degradation efficiency of BPA [51, 52]. Moreover, the presence of these two ions may also change the pH of the solution, affecting the activation of persulfate and the formation of free radicals, and further impacting the reaction environment and efficiency [53]. Overall, the Fe-MnO_2/PDS system demonstrates robust and stable performance in degrading BPA, with few limiting factors.

C. Mechanism study of BPA degradation in Fe-MnO_2/PDS system

This work introduces an AOPs system for BPA degradation, primarily driven by the non-radical sin-

DOI: 10.1063/1674-0068/cjcp2412159 © 2025 Chinese Physical Society

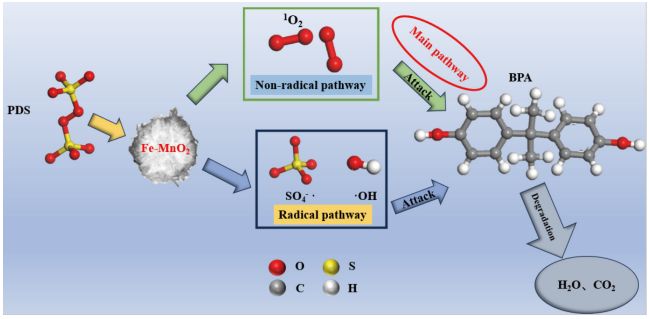

FIG. 4 The degradation mechanism diagram of Fe-MnO_2 activated PDS catalytic degradation of BPA.

glet oxygen ($^1O_2$) pathway. As illustrated in FIG. 4, within this catalytic framework, PDS molecules initially adhere to the surface of the Fe-MnO_2 catalyst. The remarkable oxidizing capability of Fe-MnO_2 then fuels the accelerated generation of both radicals (notably $SO_4^{-}\cdot$ and $\cdot OH$) and non-radicals (specifically $^1O_2$) within the reaction milieu. This elevation in concentration, particularly of $^1O_2$, enables direct oxidation and interaction with the target BPA pollutant. Consequently, this process induces structural modifications in the BPA molecule, culminating in its degradation to water and carbon dioxide. These findings align with the results obtained through quenching and EPR experiments, reinforcing the role of non-radical $^1O_2$ as the predominant reactive oxygen species in BPA degradation. Notably, although radicals such as $SO_4^{-}\cdot$ and $\cdot OH$ are present in the catalytic system, they exert a lesser influence on BPA degradation compared to $^1O_2$, yet still contribute to the overall reaction.

IV. CONCLUSION

In this study, we successfully synthesized iron-doped γ-MnO_2 hollow microspheres using a one-pot co-precipitation method. The effective incorporation of iron into the γ-MnO_2 crystal lattice was confirmed through XRD and TEM characterization, revealing no alterations to the crystal structure. This doping significantly enhanced the ability of γ-MnO_2 to activate PDS, leading to the generation of various radicals and non-radicals and subsequently improving its BPA degradation capacity. Additionally, we fine-tuned the catalytic activity of our samples by adjusting the iron doping levels, aiming to achieve peak catalytic performance. Notably, the Fe-MnO_2/PDS system demonstrated a remarkable increase in catalytic activity compared to the pure γ-MnO_2 system, with a pseudo-first-order kinetic rate constant (k value) that was nearly 100 times higher. Moreover, this system maintained robust degradation efficiency under both acidic and neutral pH conditions, with minimal ionic interference and restrictions. Our experimental findings suggest that the degradation of bisphenol A was primarily driven by the combined effects of $^1O_2$ and electron transfer. Overall, this study offers a novel approach for utilizing γ-MnO_2 catalysts in the degradation of organic pollutants within non-radical AOP systems.

Supplementary materials: XPS image of Mn in the catalyst after the reaction is shown in FIG. S1. Effects of different catalyst dosages on BPA degradation are shown in FIG. S2. Comparison of TOC removal rates between the two catalysts is shown in Table S1. The comparison of the performances of the catalysts in this article with those of the recently reported catalysts is shown in Table S2.

V. ACKNOWLEDGEMENTS

This work was financially supported by the National Natural Science Foundation of China (No.41977085), the Qing Lan Project, the 333 Project in Jiangsu Province (BRA2020300), the Six Talent Peaks Project in Jiangsu Province (2018-TD-JNHB-012).

[1] P. Martínez-Paz, M. Morales, J. L. Martínez-Guitarte, and G. Morcillo, Mutat. Res. Genet. Toxicol. Environ. Mutagen. **758**, 41 (2013).
[2] S. Ehrlich, P. L. Williams, S. A. Missmer, J. A. Flaws, K. F. Berry, A. M. Calafat, X. Ye, J. C. Petrozza, D. Wright, and R. Hauser, Environ. Health. Perspect. **120**, 978 (2012).
[3] L. Trasande, T. M. Attina, and J. Blustein, Jama **308**, 1113 (2012).
[4] O. Banerjee, S. Singh, I. Saha, S. Pal, M. Banerjee, S. Kundu, A. K. Syamal, B. K. Maji, and S. Mukherjee, Biochem. Pharmacol. **201**, 115068 (2022).
[5] K. Mokra, K. Woźniak, B. Bukowska, P. Sicińska, and J. Michałowicz, Chemosphere **201**, 119 (2018).
[6] P. Guerra, M. Kim, S. Teslic, M. Alaee, and S. Smyth, J. Environ. Manage. **152**, 192 (2015).
[7] Y. Hu, Q. Zhu, X. Yan, C. Liao, and G. Jiang, Environ. Res. **178**, 108732 (2019).
[8] Z. Pan, C. Song, L. Li, H. Wang, Y. Pan, C. Wang, J. Li, T. Wang, and X. Feng, Chem. Eng. J. **376**, 120909 (2019).

DOI: 10.1063/1674-0068/cjcp2412159 © 2025 Chinese Physical Society

[9] I. Johnson, M. A. S. Ali, and M. Kumar, *Cyanobacteria/Microalgae for Distillery Wastewater Treatment-past, Present and the Future*, Elsevier, (2019).
[10] Y. Liu, J. Guo, Y. Chen, N. Tan, and J. Wang, Environ. Sci. Technol. **54**, 14085 (2020).
[11] J. Sharma, I. Mishra, D. D. Dionysiou, and V. Kumar, Chem. Eng. J. **276**, 193 (2015).
[12] D. Dissanayake, L. A. Achola, P. Kerns, D. Rathnayake, J. He, J. Macharia, and S. L. Suib, Appl. Catal. B. **249**, 32 (2019).
[13] F. Chen, X. Jiang, L. Zhang, R. Lang, and B. Qiao, Chin. J. Catal. **39**, 893 (2018).
[14] A. R. Ribeiro, O. C. Nunes, M. F. Pereira, and A. M. Silva, Environ. Int. **75**, 33 (2015).
[15] J. Lee, U. Von Gunten, and J. H. Kim, Environ. Sci. Technol. **54**, 3064 (2020).
[16] K. Hou, Z. Pi, F. Chen, L. He, F. Yao, S. Chen, X. Li, H. Dong, and Q. Yang, ACS EST Eng. **2**, 2174 (2022).
[17] Z. Pi, K. Hou, F. Yao, L. He, S. Chen, Y. Fu, X. Li, and Q. Yang, Carbon **196**, 736 (2022).
[18] Z. Pi, K. Hou, F. Yao, L. He, S. Chen, Z. Tao, P. Zhou, D. Wang, X. Li, and Q. Yang, Chem. Eng. J. **427**, 131749 (2022).
[19] K. Hou, Z. Pi, F. Chen, L. He, F. Yao, S. Chen, X. Li, H. Dong, and Q. Yang, J. Hazard. Mater. **435**, 128970 (2022).
[20] T. Zhou, J. Du, Z. Wang, G. Xiao, L. Luo, M. Faheem, H. Ling, and J. Bao, Chem. Eng. J. Adv. **9**, 100200 (2022).
[21] M. Zhao, R. Xu, Z. Chen, Z. Gao, S. Zheng, and H. Song, Sep. Purif. Technol. **281**, 119850 (2022).
[22] X. Zhang, C. Zhang, Q. Lin, B. Cheng, X. Liu, F. Peng, and J. Ren, Front. Chem. **7**, 808 (2019).
[23] D. Barreca, F. Gri, A. Gasparotto, T. Altantzis, V. Gombac, P. Fornasiero, and C. Maccato, Inorg. Chem. **57**, 14564 (2018).
[24] Y. Zhu, M. Shen, Y. Xia, and M. Lu, Catal. Commun. **64**, 37 (2015).
[25] S. Wang, A. Guan, J. Wang, X. Fu, X. Guo, Y. Tian, K. Wang, W. Cao, and C. Zhao, B. Mater. Sci. **45**, 35 (2022).
[26] R. Yang, Y. Fan, R. Ye, Y. Tang, X. Cao, Z. Yin, and Z. Zeng, Adv. Mater. **33**, 2004862 (2021).
[27] M. Zhong, M. Li, Z. Fan, W. Huang, H. Hao, Z. Xia, Q. Zhang, H. Peng, and Y. Zhang, Chin. Chem. Lett. **34**, 107189 (2023).
[28] E. Saputra, S. Muhammad, H. Sun, A. Patel, P. Shukla, Z. Zhu, and S. Wang, Catal. Commun. **26**, 144 (2012).
[29] M. Sookhakian, H. Ullah, M. A. M. Teridi, G. B. Tong, W. J. Basirun, and Y. Alias, Sustainable Energy Fuels. **4**, 737 (2020).
[30] A. H. Mady, M. L. Baynosa, D. Tuma, and J. J. Shim, Appl. Catal. B **244**, 946 (2019).
[31] H. Liang, H. Sun, A. Patel, P. Shukla, Z. Zhu, and S. Wang, Appl. Catal. B. **127**, 330 (2012).
[32] E. L. Trainer, M. Ginder-Vogel, and C. K. Remucal, Environ. Sci. Technol. **55**, 12084 (2021).
[33] X. Zhao, Y. Bao, H. Liu, and J. Ma, Desalin. Water Treat. **144**, 263 (2019).
[34] X. Ge, X. Liu, J. Xu, X. Zheng, L. J. Tian, and X. Wang, ACS Nano **19**, 12354 (2025).
[35] J. Wang, X. Liu, Y. Shao, H. Chen, X. Zhu, X. Ge, and X. Wang, ACS EST Water **5**, 221 (2024).
[36] X. Ge, J. Wang, D. Zhou, X. Wang, and Y. Wu, Sci. China Mater. **67**, 2355 (2024).
[37] C. Wang, Y. Zeng, X. Xiao, S. Wu, G. Zhong, K. Xu, Z. Wei, W. Su, and X. Lu, J. Energy Chem. **43**, 182 (2020).
[38] W. Yang, Z. a. Su, Z. Xu, W. Yang, Y. Peng, and J. Li, Appl. Catal. B **260**, 118150 (2020).
[39] S. Sahoo, S. Zhang, and J. J. Shim, Electrochim. Acta **216**, 386 (2016).
[40] M. Jana, S. Saha, P. Samanta, N. C. Murmu, N. H. Kim, T. Kuila, and J. H. Lee, J. Power Sources **340**, 380 (2017).
[41] S. Zhu, L. Li, J. Liu, H. Wang, T. Wang, Y. Zhang, L. Zhang, R. S. Ruoff, and F. Dong, ACS Nano **12**, 1033 (2018).
[42] M. Husnah, H. A. Fakhri, F. Rohman, A. H. Aimon, and F. Iskandar, Mater. Res. Express **4**, 064001 (2017).
[43] H. Chen, Y. Wang, and Y. K. Lv, RSC Adv. **6**, 54032 (2016).
[44] L. Jin, L. Xu, C. Morein, C. H. Chen, M. Lai, S. Dharmarathna, A. Dobley, and S. L. Suib, Adv. Funct. Mater. **20**, 3373 (2010).
[45] Y. Qin, G. Li, Y. Gao, L. Zhang, Y. S. Ok, and T. An, Water Res. **137**, 130 (2018).
[46] R. Luo, M. Li, C. Wang, M. Zhang, M. A. N. Khan, X. Sun, J. Shen, W. Han, L. Wang, and J. Li, Water Res. **148**, 416 (2019).
[47] X. Ge, D. Xie, R. F. Cheng, W. Chen, C. Chen, F. Zhou, X. Wang, J. J. Chen, G. P. Sheng, and Y. Wu, Precis. Chem. **1**, 153 (2023).
[48] X. Ge, D. Zhou, J. Wang, W. Yin, X. Wang, and Y. Wu, Chem. Eng. J. **481**, 148587 (2024).
[49] J. Wang, X. Ge, W. Yin, X. Wang, and Y. Wu, Inorg. Chem. **63**, 9307 (2024).
[50] Y. Yang, J. Jiang, X. Lu, J. Ma, and Y. Liu, Environ. Sci. Technol. **49**, 7330 (2015).
[51] P. Duan, T. Ma, Y. Yue, Y. Li, X. Zhang, Y. Shang, B. Gao, Q. Zhang, Q. Yue, and X. Xu, Environ. Sci. : Nano. **6**, 1799 (2019).
[52] P. Duan, X. Liu, B. Liu, M. Akram, Y. Li, J. Pan, Q. Yue, B. Gao, and X. Xu, Appl. Catal. B **298**, 120532 (2021).
[53] Y. H. Guan, J. Ma, Y. M. Ren, Y. L. Liu, J. Y. Xiao, L. Q. Lin, and C. Zhang, Water Res. **47**, 5431 (2013).

DOI: 10.1063/1674-0068/cjcp2412159 © 2025 Chinese Physical Society